Combination of neutron imaging (NI) and digital image correlation (DIC) to determine intra-ring moisture variation in Norway spruce

Author(s):
Lanvermann, Christian; Sanabria, Sergio J.; Mannes, David; Niemz, Peter

Publication date:
2014

Permanent link:
https://doi.org/10.3929/ethz-b-000065512

Originally published in:
Holzforschung 68(1), https://doi.org/10.1515/hf-2012-0171

DOI 10.1515/hf-2012-0171 — Holzforschung 2014; 68(1): 113–122

Christian Lanvermann*, Sergio J. Sanabria, David Mannes and Peter Niemz

Combination of neutron imaging (NI) and digital image correlation (DIC) to determine intra-ring moisture variation in Norway spruce

Abstract: The hygroscopic behavior of wood has a strong influence on its mechanical performance, yet the moisture gradients within the growth ring structure have not been sufficiently investigated. The main challenge is that moisture variations are coupled with strong sample deformation, which complicates the spatial referencing of moist and dry states. In this work, neutron imaging (NI) for the detection of water and digital image correlation (DIC) for the detection of local deformation were combined to calculate the local gravimetric moisture content (MC_{grav}) and the volumetric moisture content (MC_{vol}) within single growth rings. Specimens of Norway spruce [*Picea abies* (L.) Karst.] were exposed to an adsorption-desorption cycle, with relative humidity (RH) steps varying from 0% (oven dry) up to 95% RH. After each acclimatization step, neutron transmission and DIC images were acquired. The local deformations determined by DIC were used to assign the corresponding dry density in the undeformed state to the compartment in a moist state and thus to calculate its MC by NI. No significant MC gradients could be found between earlywood (EW) and latewood (LW) within ±0.5% accuracy. However, strong density gradients between EW and LW can be directly correlated with MC_{vol}. It appears that the MC in the cell wall is constant regardless of the particular growth ring position.

Keywords: digital image correlation (DIC), gravimetric and volumetric moisture content (MC), growth rings, hygroscopic region, neutron imaging (NI), Norway spruce

***Corresponding author: Christian Lanvermann,** ETH Zurich, Institute for Building Materials, Woodphysics, Schafmattstrasse 6, 8093 Zurich, Switzerland, e-mail: lanvermannchr@ethz.ch
Sergio J. Sanabria and Peter Niemz: ETH Zurich, Institute for Building Materials, Woodphysics, Schafmattstrasse 6, 8093 Zurich, Switzerland
David Mannes: Paul Scherrer Institut, 5232 Villigen, Switzerland

Introduction

The hygroscopic behavior of wood has been studied since a long time on the microscopic and macroscopic scales. A characteristic variable is the gravimetric moisture content (MC_{grav}), defined as the mass of water per dry wood mass. Changes in MC are accompanied with swelling and shrinkage stresses, which are highly relevant for the application of wood as construction material, because the stresses can induce cracks that decrease the service life of wooden structural members (Niemz 1993). Variations in the magnitude and relation of the swelling coefficients have been observed with respect to tree species, wood density, cellulose microfibril angle, presence of reaction wood, distance from pith, and growth ring width (Kollmann and Côté 1968; May 1978; Quirk 1984; Skaar 1988; Bengtsson 2001; Badel and Perré 2002; Donaldson 2008). However, these studies have been generally conducted on macroscopic wood samples, thus neglecting the variability on the growth ring scale. For softwoods, several studies identified strong gradients between earlywood (EW) and latewood (LW) with respect to cell geometry, swelling, shrinkage, elastomechanical properties, and density (Harris and Meylan 1965; Fengel and Stoll 1973; Eder et al. 2009; Taguchi et al. 2011). High-resolution techniques (0.5–1 μm voxel size), such as micro-computer tomography, offer insight in the 3D response toward moisture changes (Trtik et al. 2007; Mannes et al. 2010; Derome et al. 2011) but are restricted to a few cell layers being simultaneously imaged. Derome et al. (2011) found pronounced anisotropic swelling and shrinkage for the low-density EW, with lowest strain in the radial direction, whereas the high-density LW showed an almost isotropic behavior. Digital image correlation (DIC) allows observing the local surface deformation, not only of a few cells but also of larger areas, with recent developments in user-friendliness and accuracy (Valla et al. 2010; Hansmann et al. 2011). Recent investigations confirmed a pronounced correlation between wood density and moisture-induced radial deformation (Keunecke et al. 2012).

Only a few studies have addressed the question whether gradients of MC_{grav} exist within the annual ring. Early investigations indicated 0.9% higher MC_{grav} in LW than in EW for Scots pine (*Pinus sylvestris*) (Boutelje 1962) and fir (*Abies alba*) (Popper and Bariska 1972). Pang and Herritsch (2005) found a MC_{grav} increase of 0.1% to 0.6% for Radiata pine (*Pinus radiata*) and attributed this to an increased content in hemicelluloses. Moon et al. (2010) found a MC_{grav} increase of 1% for Loblolly pine (*Pinus taeda*). However, the aforementioned investigations were carried out on isolated samples of EW and LW. Recently, Dvinskikh et al. (2011) and Eitelberger et al. (2011a) measured bound water in the hygroscopic region along full annual ring profiles by magnetic resonance imaging (MRI). A direct proportionality was found between cell wall density and local water concentration, which was interpreted as an even moisture distribution within the cell wall. MRI does not require deformation compensation due to the simultaneous measurement of local water and dry density of cell wall polymers from the moist state. The main drawback is the measurement time, due to the pointwise testing scheme, which is generally restricted to single profiles. An alternative nondestructive technique is neutron imaging (NI). NI was only recently applied for wood research (Lehmann et al. 2001a; Mannes et al. 2009a; Lehmann and Mannes 2012). In addition to its high sensitivity toward some light elements such as hydrogen, NI allows for full-field imaging of time-dependent processes with second time resolution while at the same time providing submillimeter spatial resolution. This makes it suitable for the detection of bound water during diffusion (Mannes et al. 2009b; Sonderegger et al. 2010) or the radial moisture transport during drying (Rosner et al. 2012). However, due to the significant inhomogeneous deformation in radial and tangential directions, a specific local position in a moist state cannot be directly assigned to the same position in the dry condition (i.e., additional referencing information is required between moist and dry images).

This problem is addressed here: NI and DIC will be combined to provide simultaneously data sets on MC and local deformation. These data sets, referenced to the dry state of the sample, enable the simultaneous full-field calculation of the local MC_{grav} and deformation. Norway spruce samples were subjected to a full adsorption and desorption cycles. The MC_{grav}, MC_{vol}, and moisture-induced strain were calculated as a function of the local growth ring position for each relative humidity (RH) step.

Materials and methods

Wood samples

A total of four 40×40×5 mm^3 (R×T×L) samples were cut from a stem of Norway spruce [*Picea abies* (L.) Karst.] at 1 m above ground (Lanvermann et al. 2013). Growth rings with low curvature and well aligned with the samples were chosen. This sample size affords a large RT-surface and the equilibrium moisture content (EMC) can be obtained within a short time due to the high diffusion coefficient in the longitudinal direction. The mean growth ring width was 2.81 mm at a mean density of 362 kg m^{-3}.

A random speckle pattern was applied on one of the RT-surfaces as a reference for the strain calculation with DIC. A water-based color was sprayed in two steps (airbrush gun with a nozzle size of 0.2 mm): first, a white background, and second, a fine randomly distributed black foreground. The samples were dried at 103°C and kept in sealed plastic bags and covered with silica gel; the assembly was covered with a second plastic bag to prevent moisture changes before experiments at the NI facility.

Experimental setup

Instrument: thermal neutron beamline NEUTRA (Lehmann et al. 2001b) situated at the Paul Scherrer Institut (Villigen, Switzerland). The setup consists of the NI system, the DIC setup, and a climate box with air stream regulation (Figure 1). The neutron radiography method was described by Lehmann et al. (2001a) and Mannes et al. (2009a,b). The imaging detector is a ^{6}LiF:ZnS scintillator (thickness, 100 µm), which converts neutron radiation into visible light, being subsequently reflected by a mirror onto a CCD camera with a resolution of 2048×2048 $pixel^2$. The digital pixel size was 154 µm and the

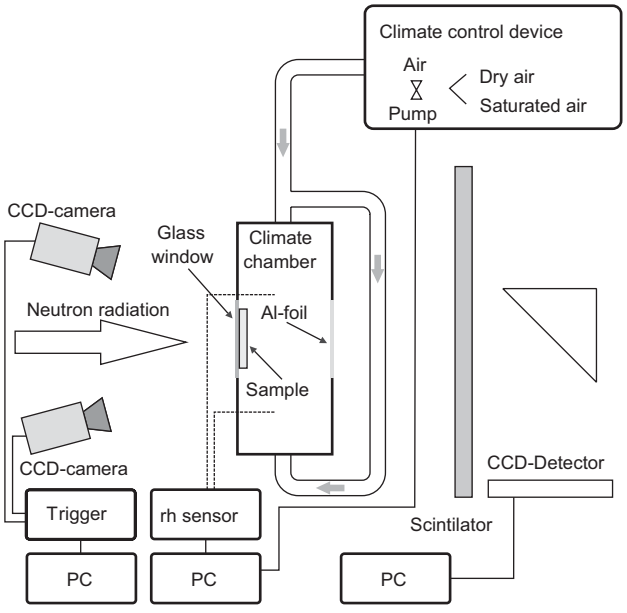

Figure 1 Schematic of experimental setup.

field of view was approximately 315 mm. The exposure time for the images was 22 s.

The DIC images were acquired by a commercial VIC3D System (Correlated Solutions, Columbia, SC, USA). Two CCD cameras were used with a digital pixel size of approximately 70 µm, which were covered with lead sheets to shield the electronics from neutron radiation. The setup was illuminated with two cold-light sources (color temperature, 5000 K).

The samples were stored in a climate box that serves two purposes: (1) it defines the humidity-controlled volume and (2) it allows for a reproducible sample orientation perpendicular to the neutron beam path. The front of the climate box is equipped with a glass window to allow for optic measurement with DIC. The backside foil of the box and the sample holder are made of aluminum, known to be almost transparent for neutron radiation (Figure 1). The acclimatization of the box is achieved by mixing dry and moist air streams (Derome et al. 2011). The samples were stored in the lower part for a minimum of 6 h. The following nominal RH states were consecutively investigated: adsorption (RH): 0% (reference state), 15%, 30%, 45%, 65%, 75%, 90%, and 95%; desorption (RH): 90%, 75%, 65%, 45%, 30%, 15%, and 0%.

After each 6 h conditioning period, the weight of the samples was gravimetrically measured (Mettler-Toledo, Greifensee, Switzerland; 0.01 g precision). The samples were then positioned in a slotted aluminum profile, and the NI radiographies and DIC optic images were acquired. This procedure was repeated for all RH states and samples.

Deformation compensation (Figure 2)

First, the grayscale values of the raw NIs were corrected by standard procedures for inhomogeneities in the detector and neutron beam, background, and sample scattering (Mannes et al. 2009a). The commercial correlation software (VIC3D version 2007; Correlated Solutions) was used to calculate the in-plane deformation fields (u, v) with respect to the initial dry image coordinates (x, y), together with the strain fields $\varepsilon_{xx}=\partial_x u$, $\varepsilon_{yy}=\partial_y v$, and $\varepsilon_{xy}=0.5\,(\partial_y u+\partial_x v)$.

The NIs were aligned with respect to each other and to the calculated deformation fields with self-developed software based on the image processing packages of MATLAB (The Mathworks, Inc., Natick, MA, USA). In a first step, the optic (2.1 and 2.2) and neutron stacks (2.3) were independently prealigned with respect to the dry state to compensate for positioning uncertainties and vibration of cameras, neutron radiography, and sample positioning systems. Six steel screws Si={S1, S2, . . ., S6} distributed around the sample field of view served as reference markers for image registration. In the optic stacks, the heads of the screws appear as surface reflectors with varying illumination, which are binarized with Otsu's method followed by a centroid detection (2.4); in the neutron stacks, the integrated transmission patterns at screw regions are optimally tracked by maximizing the 2D cross-correlation with respect the reference image (2.5) (Gonzalez et al. 2004). In a second step, the neutron and optic stacks were aligned with respect to their marker

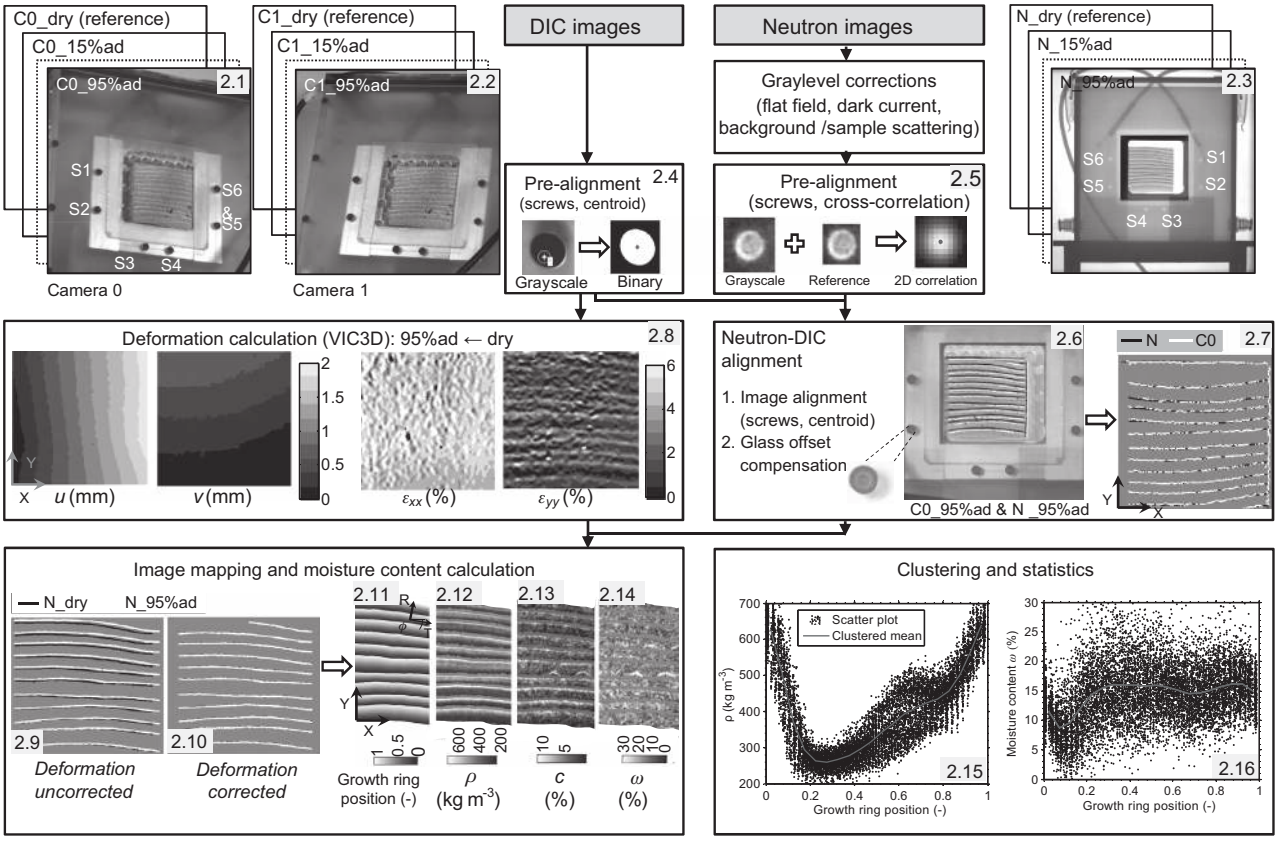

Figure 2 Data processing flowchart for DIC and NIs together with sample outputs (2.1, . . ., 2.16) of the main evaluation steps.

centroids (2.6). The transformation between control point pairs in reference images (x_{Si}, y_{Si}) and aligned images $(\hat{x}_{Si}, \hat{y}_{Si})$ was in each step described with a projective mapping, which defines a general 2D projection of a 3D scene for a pin-hole camera model (Sutton et al. 2009):

$$\begin{aligned}\hat{x}_{Si} &= \left(h_{11}\,x_{Si}+h_{12}\,y_{Si}+h_{13}\right)\left(h_{31}\,x_{Si}+h_{32}\,y_{Si}+h_{33}\right)^{-1}\\ \hat{y}_{Si} &= \left(h_{21}\,x_{Si}+h_{22}\,y_{Si}+h_{23}\right)\left(h_{31}\,x_{Si}+h_{32}\,y_{Si}+h_{33}\right)^{-1},\end{aligned} \tag{1}$$

where the elements of the transformation matrix h_{ij} are uniquely determined by four control point pairs. The two additional markers allowed reduction of position uncertainties by fitting with linear least squares in Equation (1) and provided a position error estimate. In the second alignment step, for example, the h_{ij} with minimum fitting error was chosen from several fittings calibrated with selected reference images. Because the centroid detection is influenced by the marker geometry (Heikkilä and Silvén 1997), the second alignment step was repeated twice to achieve consistent marker geometry in both neutron and optic stacks.

A comparison of the aligned neutron and optic stacks (2.6) reveals an offset in the wood sample position, which was associated to the perspective effect and light refraction introduced by the l_g=1.5 mm thick glass window at the front of the climate box (Figure 3). The offset was approximated with a constant for all images, which was averaged along the displacements (Δ_X, Δ_Y) over the field of view simulated in function of the camera distance D_z=0.8 m and inclination (α_X, α_Y)=(22°, 18°) and the refraction indexes of air (n=1.0) and glass (n'=1.5):

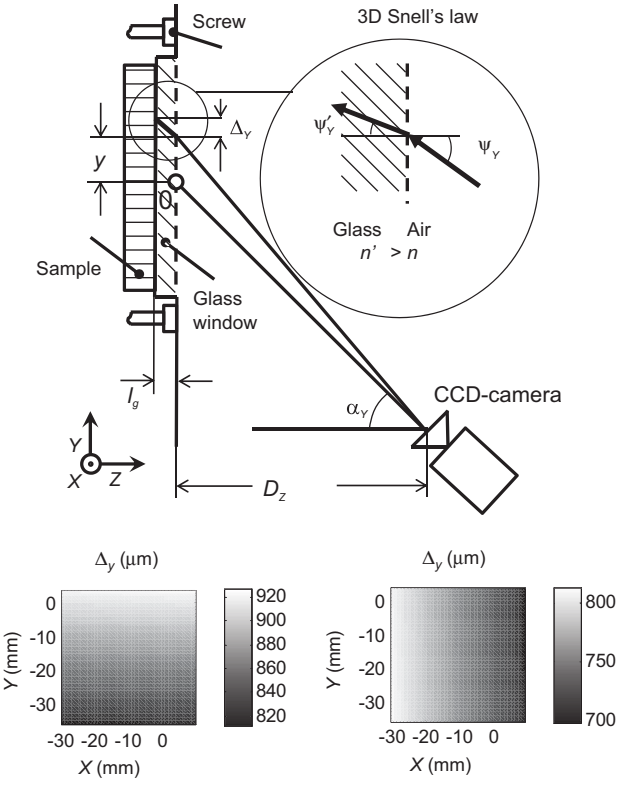

Figure 3 Characterization of inhomogeneous offset (Δ_X, Δ_Y) between DIC and NIs due to front glass window of climate box.

$$\begin{aligned}\Delta_{\{X,Y\}} &= l_g \tan\psi'_{\{X,Y\}}\\ \psi'_{\{X,Y\}} &= \arcsin\left[\sin\psi_{\{X,Y\}}\left(n/n'\right)\left\{1+\tan^2\psi_{\{Y,X\}}\cos^2\theta_{\{X,Y\}}\left[1-\left(n/n'\right)^2\right]\right\}^{-1/2}\right]\\ \psi_{\{X,Y\}} &= \tan^{-1}\left(\tan\alpha_{\{X,Y\}}+y/D_z\right),\end{aligned} \tag{2}$$

Equation (2) is an extension of the equation of Eitner et al. (2010), combining trigonometric considerations with a 3D expression of Snell's refraction law. Figure 2 shows the images after offset compensation (2.7), and the sample edges and LW/EW transitions appear at consistent positions.

Finally, the VIC3D deformation fields (u, v) (2.8) were compensated for the NIs to reference specific moist states. Figure 2 shows the LW/EW transitions in moist (95% Ad.) and dry NIs before (2.9) and after (2.10) deformation correction. The moistening leads to visible year ring swelling, especially in the tangential direction, which is compensated for in the corrected images. Bicubic interpolation was used to minimize noise, and all above-described image transformation steps were grouped into a single coordinate transformation.

Calculation of MC_{grav} and MC_{vol}

The deformation-corrected images were mapped and the local dry wood density ρ_w (2.12), volumetric moisture content (MC_{vol}) (2.13), and MC_{grav} (2.14) were calculated according to Lambert-Beer's law for each pixel. The equations of Mannes et al. (2009b) were extended to account for the heterogeneous deformation of the pixel dimensions in dry state (dx, dy) to a size $(d\hat{x}, d\hat{y})=\left(dx\left[1+\varepsilon_{xx}\right], dy\left[1+\varepsilon_{yy}\right]\right)$ in the moist state. The swelling results in a lower effective density of wood substance in the moist state for the same pixel size. MC_{grav} is expressed as the water mass in the deformed pixel (m_h) over the dry wood mass:

$$\begin{aligned}MC_{grav} &= m_h/m_w = \rho_h Z_h\, d\hat{x}d\hat{y}/\left(\rho_w l_z\, dxdy\right)\\ &= \left(1+\varepsilon_{xx}\right)\left(1+\varepsilon_{yy}\right)\rho_h Z_h/\left(\rho_w l_z\right),\end{aligned} \tag{3}$$

where z_h is the effective water column length in the moist state, l_z is the initial sample thickness, and ρ_h and ρ_w are the densities of water and dry wood substance, respectively. MC_{vol} is calculated as the volume of water (V_h) over the total volume (V_u) of the moist sample:

$$MC_{vol} = V_h/V_u = z_h/[l_z\,(1+\varepsilon_{zz})] \approx z_h/l_z. \tag{4}$$

The out of plane strain ε_{zz} in the fiber direction was very small (15 µm for an expected maximum swelling coefficient of 0.3%) (Kollmann and Côté 1968) and thus not considered. z_h is expressed as a function of the neutron parameters with:

$$z_h = -1/\Sigma_h\,\{\ln T - \ln T_0/[(1+\varepsilon_{xx})\,(1+\varepsilon_{yy})]\}, \tag{5}$$

where Σ_h is the neutron attenuation coefficient of water and T and T_0 are the open-beam normalized neutron transmission through moist and dry wood, respectively. ρ_w is expressed as a function of the mass-attenuation coefficient of wood $(\Sigma/\rho)_w$ and l_z:

$$\rho_w = -\ln T_0\,[(\Sigma/\rho)_w l_z]^{-1}. \tag{6}$$

The calculated quantities were plotted as a function of the relative growth ring position $\varphi(0, \ldots, 1)$, with 0 and 1 defining EW and LW regions.

φ is calculated by segmenting and fitting to cubic smoothing splines the LW-EW transitions in the dry reference NIs, and the slope of the spline provides the annual ring angle ϕ. The strain fields calculated with VIC3D (ε_{xx}, ε_{yy}) are then referred to the material directions R and T with

$$\varepsilon_{\{TT,\,RR\}} = \varepsilon_{XX}\cos^2\phi + \varepsilon_{YY}\sin^2\phi \pm 2\,\varepsilon_{XY}\cos\phi\sin\phi. \quad (7)$$

Figure 2 shows scatter plots for the point-to-point mapping of ρ_w (2.15) and MC_{grav} (2.16) with ϕ. Considerable random noise is available due to both the remaining background noise in the NIs and the natural variability among the investigated annual rings of the tested sample. To create smooth trends between the test quantities, the clustering procedure described by Sanabria et al. (2013) was applied to the scatter plots. φ was clustered into 0.05 long intervals, for which the mean value was calculated (~4500 averages per cluster).

Results and discussion

MC and influence of deformation compensation

The gravimetrically determined MC ω, plotted as the mean of four samples against the RH, is shown in Figure 4. The hysteresis behavior is clearly reflected between adsorption and desorption. However, when comparing the mean sorption isotherm with a mean isotherm calculated with the Hailwood-Horrobin model (values from Popper and Niemz 2009), they are 2% to 3% lower for the whole humidity range. The most likely explanation for this can be found in the relatively short acclimatization time of 6 h per RH step. The acclimatization time of 6 h step did not lead to fully equilibrated samples, although the sample thickness of 5 mm was chosen, which, in view of a mean tracheid length in Norway spruce of 2.8 mm (Wagenführ 2000), should lead to a good accessibility of the open lumen and the equilibrium should be achieved under ambient conditions within short time. However, due to the sample orientation with the smallest dimension parallel to the longitudinal direction, no effective moisture profiles are visible in the images. An additional factor to decrease EMC can be found in the prior drying treatment of the samples at 103°C that reportedly leads to slightly reduced EMC (e.g., Kollmann and Côté 1968; Niemz 1993).

When comparing MC_{grav} ω with those obtained by MC_{NI} as the mean of the evaluated sample surface (Figure 5), the values are in good agreement as indicated by a linearly fitted slope of 0.9445 and a coefficient of determination of 0.9714. This demonstrates the overall applicability of the NI procedure for MC determination, however, within an uncertainty range of ±2% as indicated by the scattered data. The effect of neglecting the strain terms ε_{xx} and ε_{yy} in Equation (2) results in an additional MC deviation of up to 6% with respect to the reference MC_{grav} (Figure 5) and also increases the intra-ring variation from ±0.5% to ±1.5% (data not shown). Therefore, the strain information cannot be neglected in the local MC_{grav} computation.

Confrontation of volumetric and gravimetric MC and strain

The complete data (i.e., local dry density, MC_{vol} and MC_{grav} for 65% and 95% RH and the corresponding radial and

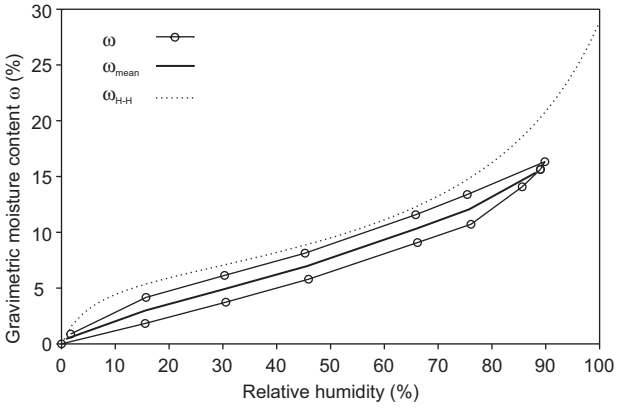

Figure 4 Gravimetrically determined sorption isotherm for adsorption and desorption (hollow circles), mean sorption isotherm (bold line), and computed mean sorption isotherm (dashed line) calculated according to the Hailwood-Horrobin model (Popper and Niemz 2009).

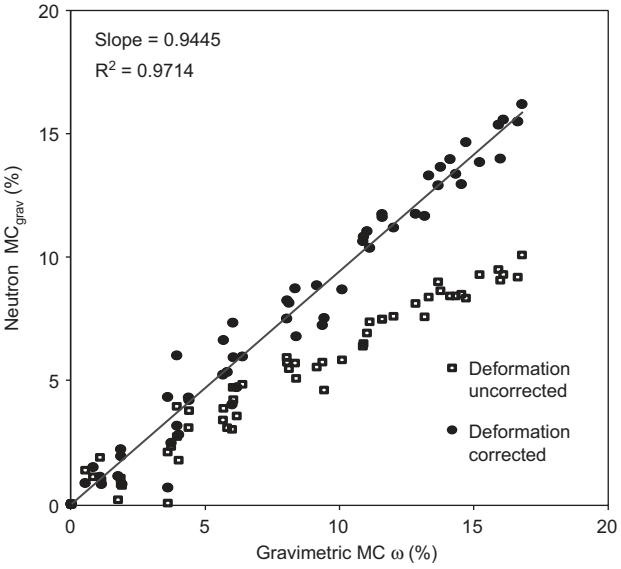

Figure 5 Comparison between MC_{grav} and mean MC determined with NI (MC_{NI}) with and without deformation correction.

tangential strains) of a representative sample are given in Figure 6. The pronounced radial density gradients are found within the growth rings (Figure 6a), with a minimum density of approximately 250 to 300 kg m^{-3} in the EW regions, which increases to a maximum of approximately 600 to 800 kg m^{-3} in the LW regions and abruptly drops to the next EW. These densities fairly agree with those reported in the literature (Wagenführ 2000; Keunecke et al. 2012). The observed peak values are influenced by the effective lateral resolution of the NIs (~700 µm), which results in a smoothing of the density profiles. The MC_{vol}, as displayed in Figure 6b for 65% and 95% RH, shows a strong correlation with the density within the growth rings. Whereas the low-density EW regions show a MC_{vol} of 3% to 4%, the high-density LW regions show about twice the MC_{vol} (8–10%) at 95% RH. Whereas density and MC_{vol} are closely interrelated, MC_{grav} shows a different behavior (Figure 6c). The individual growth rings seem to be characterized by a roughly constant MC_{grav} throughout the center portion of the rings and sudden drops around the growth ring boundary regions. Additional oscillations are found for the narrow growth rings at sample positions 7 and 14 mm. When accounting for the corresponding radial and tangential strain pattern for the 95% RH state as presented in Figure 6d, radial strain shows a strong correlation with density, where the lowest strains are found for EW (~1%) with a continuous increase toward LW (3–4%). At the same time, the tangential strain is fairly constant (~5.5%) over the evaluated area. Again, the lateral resolution especially influences the radial strain maxima, and in the case of DIC, where the smoothing is an integral part of the procedure, it can be minimized but cannot be eliminated completely (Valla et al. 2010; Keunecke et al. 2012).

The occurrence of MC_{grav} drops at the LW-EW interfaces can be numerically reproduced (Figure 7) by artificially incorporating smoothing to ideal neutron transmission profiles. T and T_o are simulated by backward solving Equations (3) to (6) for high-resolution (~70 µm) density profiles, which were experimentally determined by X-ray densitometry (Evans 1994; Evans et al. 1999). Thus, ideally constant MC_{grav} profiles (dashed lines) can be obtained, which are influenced by random noise, positioning uncertainties, and smoothing and the subsequently recalculated MC_{grav} and ρ_w are represented by solid lines. The

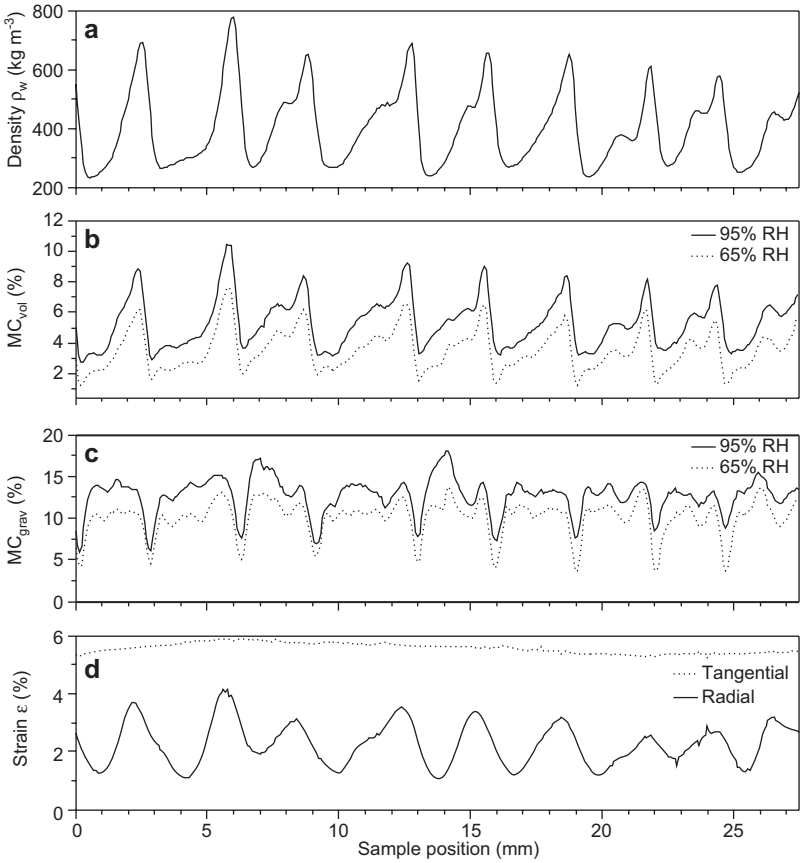

Figure 6 Oven-dry density ρ_w (a), MC_{vol} (b), MC_{grav} (c), and corresponding radial and tangential strain ε (d) over a sample. MC_{grav} drops at growth ring boarders are artifacts due to smoothing effects and do not reflect physical reality.

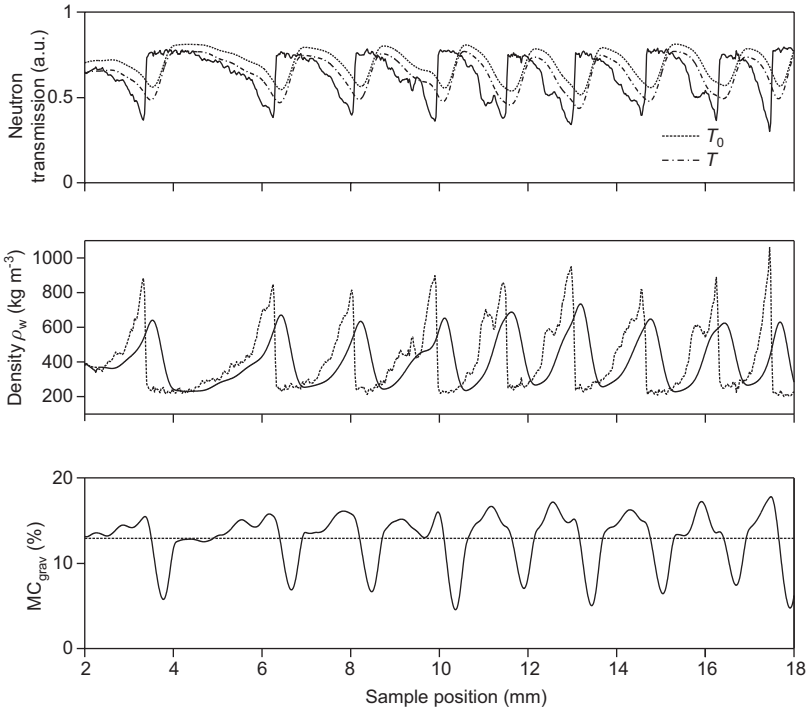

Figure 7 Simulation of effect positioning uncertainties, NI lateral resolution, and background noise on MC determination. NI normalized transmission in dry and moist state T_0, T are backward solved for a flat MC and a high-resolution density profile (dashed lines). Density ρ_w and MC_{grav} are recalculated (solid lines) after adding up experimental uncertainties (Table 1).

simulated MC_{grav} trends (Figure 7) are in fair agreement with the experiments (Figure 6), which shows that the aforementioned effects are most likely measurement artifacts than physical reality.

Measurement uncertainty and improvements

Despite the good correlation between mean NI MC_{grav} values and those determined by gravimetry, there are uncertainties in the NIs due to artifacts related to positioning uncertainties, the limited lateral resolution, and background noise (Table 1). The most important contribution to the former is the NI-DIC registration due to the front glass distortion (Figure 3). A possible approach for improvement is the compensation of inhomogeneous offset fields (Haile and Ifju 2012). The out-of-plane displacements (misalignment and swelling) are small, which allows simplifying the DIC setup to a single camera (2D correlation) with MC_{grav} deviations below 0.2% (mean square error). The smoothing artifacts (Figures 6 and 7) are mainly a consequence of the limited lateral resolution of NIs. Reducing positioning uncertainties by a factor of 10 reduces MC_{grav} drops only by 2. The DIC subset size is not critical, and a reduction from the 15-pixel subset used here for DIC correlation to a 9-pixel subset led to <0.07% changes in MC_{grav} along the full φ range while reducing the evaluable sample area. Overall, the lateral resolution of NI is a compromise with the sample size, and a lateral resolution of approximately 150 µm has been achieved with 1-mm-thick samples (Mannes et al. 2007). As for noise in the NI images, the main contribution is the remaining background scattering of the climate box, caused especially by the lateral walls (Plexiglass). There is a place for optimization of the box construction with neutron-transparent materials (e.g., glass and aluminum).

Table 1 List of main uncertainty sources influencing NI/DIC moisture measurements.

Positioning uncertainties (SD)	µm
Alignment with screw markers	50
Out-of-plane errors	30
Glass offset effect	80
VIC3D	6
Lateral resolution (5–95% slope)	µm
NIs	700
VIC3D subset size	600
Background noise (SD)	% in T, T_0
NIs	2%

Intra-ring MC variation

The growth rings of all samples were aligned and their mean properties were calculated to minimize the aforementioned artifacts and to present a more general view of the correlation between local oven-dry density within a growth ring and corresponding MC_{grav}. The resulting density and MC_{grav} curves for the RHs are presented for adsorption in Figure 8 as a function of the normalized growth ring position φ. As stated before, the sharp transition at the growth ring boundary is artifact prone. Therefore, φ values from 0 to 0.3 (depicted as gray area) are omitted from the discussion. The density progression in the growth rings (Figure 8a) can be simplified with two straight lines. The density increases from approximately 275 kg m^{-3} in EW until a relative growth ring position of approximately 0.8 and then the slope abruptly increases toward the end of the growth ring, where the maximum density of approximately 600 kg m^{-3} is reached. The individual RH (Figure 8b) steps can be clearly separated with respect to MC_{grav}, where an increasing RH leads to a higher mean MC_{grav}. They are fairly constant for all φ with a slight variation of ±0.5%. However, this variation seems to be reproducible for all displayed RH steps during adsorption as well as for desorption (data not shown), except for the 65% RH. From the EW (φ=0.3) the MC_{grav} shows local maxima at approximately φ=0.5 and 0.9, coinciding to changes in slope in the LW density, which are similarly associated to spatial smoothing artifacts. Under consideration of the total uncertainty between MC_{NI} and MC_{grav} (Figure 4) and the MC trends of Figure 6, it can be concluded that the MC_{grav} is constant within the growth ring within a ±0.5% uncertainty range. Smaller MC_{grav} variations fall below the measurement uncertainty and cannot be reliably attributed to a physical effect.

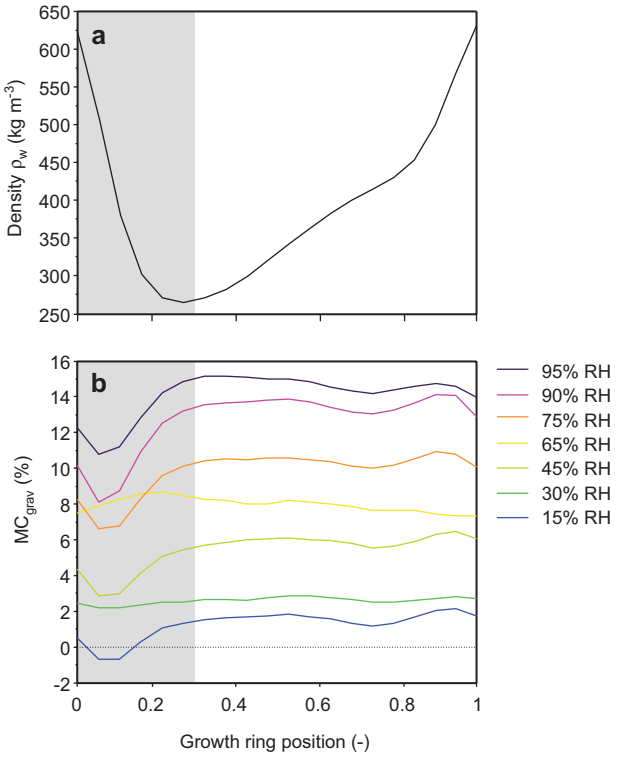

Figure 8 Dry density ρ_w and MC_{grav} in adsorption for different RH states depending on position within growth ring. 0 denotes EW and 1 denotes LW. Growth ring position from 0 to 0.3 (gray rectangle) is an artifact and is therefore excluded from evaluation.

A clear distinction has to be made between MC_{vol} and MC_{grav}. MC_{vol} has a strong correlation with density as demonstrated by nuclear magnetic resonance spectroscopy for steady-state moisture diffusion (60% RH difference) in radial direction with high MC_{vol} in the dense LW and low MC_{vol} in the light EW (Eitelberger et al. 2011a). Similar results were found for *P. sylvestris* by other authors (Hameury and Sterley 2006; Dvinskikh et al. 2011; Eitelberger et al. 2011b). Clearly, our data further support these observations under equilibrium conditions. Whereas the MRI method of Dvinskikh et al. (2011) and Eitelberger et al. (2011b) achieves a better lateral resolution (78 µm) and consequently gives rise to a larger artifact-free year ring portion, the combined NI and DIC measurements allow full-field *in situ* monitoring of combined moisture and deformation processes, providing both MC_{vol} and MC_{grav} in addition to the corresponding deformations.

The general conclusion drawn from the observed flat MC_{grav} trend is that the amount of water in a given volume of cell wall material is approximately constant regardless of the growth ring position. However, the total MC_{vol} is significantly higher in LW than in EW due to its thicker cell walls, which are reflected in the overall higher density. This plays an important role when accounting for wood hygromechanical properties, which show a strong correlation with MC_{grav} (Gerhards 1982). Furthermore, in the hygroscopic region (below fiber saturation point), the relation between RH and swelling of bulk wood is known to be linear (Kollmann and Côté 1968). From our observations, this relation seems to be also true at the growth ring scale. The higher MC_{vol} in LW is accompanied by a higher deformation of the compartment, which leads to a constant MC_{grav}.

Conclusion

The question was in focus, in which relation are the parameters MC_{grav}, cell geometry, density, and elastic properties within the growth rings of Norway spruce. The method

tested, which combines NI and DIC, shows promising features because it allows for calculating the local MC_{grav} and MC_{vol}. The local MC_{vol} is strongly influenced by the oven-dry density, but the MC_{grav} is constant within a range of ±0.5% in the hygroscopic region. Unfortunately, the region φ=0, …, 0.3 in the vicinity of LW-EW interfaces is artifact prone and cannot be interpreted safely. The agreement between MC_{grav} and MC_{NI} values for individual samples is ±2%. The swelling strains need to be included in the MC_{grav} calculations; otherwise, the error would be ±5%. The combination of NI and DIC permits the simultaneous analysis of moisture distribution and deformation in materials. The method could be useful for the observation of time-dependent sorption behavior and drying. The NI+DIC method is rapid with data acquisition in a few seconds and permits the simultaneous computation of strain and moisture related quantities. After further improvements, which could involve a simplification of the method by using solely the NI images for cross-correlation and an improved referencing frame, it could be an alternative for the study of moisture transport and deformation in wood.

Acknowledgments: The first author financed by the Swiss National Science Foundation (Grant No. 125184). The Building Physics group at EMPA is acknowledged for using the conditioning device. Furthermore, Ms. V. Krackler and Mr. F. Michel are gratefully acknowledged for helping with the experiments at Paul Scherrer Institut, and Dr. Falk Wittel for his contribution in the data evaluation.

Received October 23, 2012; accepted March 25, 2013; previously published online May 4, 2013

References

Badel, É., Perré, P. (2002) Predicting oak wood properties using X-ray inspection: representation, homogenisation and localisation. Part I: digital X-ray imaging and representation by finite elements. Ann. For. Sci. 59:767–776.

Bengtsson, C. (2001) Variation of moisture induced movements in Norway spruce (*Picea abies*). Ann. For. Sci. 58:568–581.

Boutelje, J.B. (1962) The relationship of structure to transverse anisotropy in wood with reference to shrinkage and elasticity. Holzforschung 16:33–46.

Derome, D., Griffa, M., Koebel, M., Carmeliet, J. (2011) Hysteretic swelling of wood at cellular scale probed by phase-contrast X-ray tomography. J. Struct. Biol. 173:180–190.

Donaldson, L. (2008) Microfibril angle: measurement, variation and relationships – a review. IAWA J. 29:345–386.

Dvinskikh, S.V., Henriksson, M., Berglund, L.A., Furó, I. (2011) A multinuclear magnetic resonance imaging (MRI) study of wood with adsorbed water: estimating bound water concentration and local wood density. Holzforschung 65:103–107.

Eder, M., Jungnikl, K., Burgert, I. (2009) A close-up view of wood structure and properties across a growth ring of Norway spruce (*Picea abies* [L] Karst.). Trees-Struct. Funct. 23:79–84.

Eitelberger, J., Hofstetter, K., Dvinskikh, S.V. (2011a) A multi-scale approach for simulation of transient moisture transport processes in wood below the fiber saturation point. Compos. Sci. Technol. 71:1727–1738.

Eitelberger, J., Svensson, S., Hofstetter, K. (2011b) Theory of transport processes in wood below the fiber saturation point. Physical background on the microscale and its macroscopic description. Holzforschung 65:337–342.

Eitner, U., Köntges, M., Brendel, R. (2010) Use of digital image correlation technique to determine thermomechanical deformations in photovoltaic laminates: measurements and accuracy. Sol. Energy Mater. Sol. C 94:1346–1351.

Evans, R. (1994) Rapid measurement of the transverse dimensions of tracheids in radial wood sections from *Pinus radiata*. Holzforschung 48:168–172.

Evans, R., Hughes, M., Menz, D. (1999) Microfibril angle variation by scanning X-ray diffractometry. Appita J. 52:363–367.

Fengel, D., Stoll, M. (1973) Über die Veränderungen des Zellquerschnitts, der Dicke der Zellwand und der Wandschichten von Fichtenholz-Tracheiden innerhalb eines Jahrringes. Holzforschung 27:1–7.

Gerhards, C.C. (1982) Effect of moisture content and temperature on the mechanical properties of wood: an analysis of immediate effects. Wood Fiber Sci. 14:4–36.

Gonzalez, R.C., Woods, R.E., Eddins, S.L. Digital Image using Matlab Processing. Pearson Prentice-Hall, Upper Saddle River, 2004.

Haile, M.A., Ifju, P.G. (2012) Application of elastic image registration and refraction correction for non-contact underwater strain measurement. Strain 48:136–142.

Hameury, S., Sterley, M. (2006) Magnetic resonance imaging of moisture distribution in *Pinus sylvestris* L. exposed to daily indoor relative humidity fluctuations. Wood Mater. Sci. Eng. 1:116–126.

Hansmann, C., Konnerth, J., Rosner, S. (2011) Digital image analysis of radial shrinkage of fresh spruce (*Picea abies* L.) wood. Wood Mater. Sci. Eng. 6:2–6.

Harris, J.M., Meylan, B.A. (1965) The influence of microfibril angle on longitudinal and tangential shrinkage in *Pinus radiata*. Holzforschung 19:144–153.

Heikkilä, J., Silvén, O. (1997) A four-step calibration procedure with implicit image correction. In: Proceedings of the IEEE Computer Society Conference on Computer Vision and Pattern Recognition, pp. 1106–1112.

Keunecke, D., Novosseletz, K., Lanvermann, C., Mannes, D., Niemz, P. (2012) Combination of X-ray and digital image correlation for the analysis of moisture-induced strain in wood: opportunities and challenges. Eur. J. Wood Wood Prod. 70:407–413.

Kollmann, F.F., Côté, W.A. Principles of Wood Science and Technology: Part I Solid Wood. Springer Verlag, 1968.

Lanvermann, C., Schmitt, U., Evans, R., Hering, S., Niemz, P. (2013) Distribution of structure and lignin within growth rings of Norway spruce. Wood Sci. Technol. Published online first. DOI: 10.1007/s00226-013-0529-8.

Lehmann, E.H., Mannes, D. (2012) Wood investigations by means of radiation transmission techniques. J. Cult. Herit. 13:35–43.

Lehmann, E.H., Vontobel, P., Scherrer, P., Niemz, P. (2001a) Anwendung der Methode der Neutronenradiographie zur Analyse von Holzeigenschaften. Eur. J. Wood Wood Prod. 59:463–471.

Lehmann, E.H., Vontobel, P., Wiezel, L. (2001b) Properties of the radiography facility NEUTRA at SINQ and its potential for use as a European Reference Facility. Nondestr. Testing Eval. 16:191–202.

Mannes, D., Lehmann, E., Cherubini, P., Niemz, P. (2007) Neutron imaging versus standard X-ray densitometry as method to measure tree-ring wood density. Trees 21:605–612.

Mannes, D., Josic, L., Lehmann, E., Niemz, P. (2009a) Neutron attenuation coefficients for non-invasive quantification of wood properties. Holzforschung 63:472–478.

Mannes, D., Sonderegger, W., Hering, S., Lehmann, E., Niemz, P. (2009b) Non-destructive determination and quantification of diffusion processes in wood by means of neutron imaging. Holzforschung 63:589–596.

Mannes, D., Marone, F., Lehmann, E., Stampanoni, M., Niemz, P. (2010) Application areas of synchrotron radiation tomographic microscopy for wood research. Wood Sci. Technol. 44:67–84.

May, H. (1978) Einflüsse von Rohdichte und Jahrringbreite auf das Quellungsverhalten von Fichten-und Kiefernholz. Eur. J. Wood Wood Prod. 36:199–202.

Moon, R.J., Wells, J., Kretschmann, D.E., Evans, J., Wiedenhoeft, A.C., Frihart, C.R. (2010) Influence of chemical treatments on moisture-induced dimensional change and elastic modulus of earlywood and latewood. Holzforschung 64:771–779.

Niemz, P. Physik des Holzes und der Holzwerkstoffe. DRW, Leinfelden-Echterdingen, 1993.

Pang, S., Herritsch, A. (2005) Physical properties of earlywood and latewood of *Pinus radiata* D. Don: anisotropic shrinkage, equilibrium moisture content and fibre saturation point. Holzforschung 59:654–667.

Popper, R., Bariska, M. (1972) Die Azylierung des Holzes – Erste Mitteilung: Wasserdampf-Sorptionseigenschaften. Eur. J. Wood Wood Prod. 3:289–294.

Popper, R., Niemz, P. (2009) Wasserdampfsorptionsverhalten ausgewählter heimischer und überseeischer Holzarten. Bauphysik 31:117–121.

Quirk, J. (1984) Shrinkage and related properties of Douglas-fir cell walls. Wood Fiber Sci. 16:115–133.

Rosner, S., Riegler, M., Vontobel, P., Mannes, D., Lehmann, E.H., Karlsson, B., Hansmann, C. (2012) Within-ring movement of free water in dehydrating Norway spruce sapwood visualized by neutron radiography. Holzforschung 66:751–756.

Sanabria, S.J., Hilbers, U., Neuenschwander, J., Niemz, P., Sennhauser, U., Thömen, H., Wenker, J.L. (2013) Modeling and prediction of density distribution and microstructure in particleboards from acoustic properties by correlation of non-contact high-resolution pulsed air-coupled ultrasound and X-ray images. Ultrasonics 53:157–170.

Skaar, C. Wood-Water Relations. Springer-Verlag, Heidelberg, 1988.

Sonderegger, W., Hering, S., Mannes, D., Vontobel, P., Lehmann, E.H., Niemz, P. (2010) Quantitative determination of bound water diffusion in multilayer boards by means of neutron imaging. Eur. J. Wood Wood Prod. 68:341–350.

Sutton, M.A., Orteu, J.J., Schreier, H.W. Image Correlation for Shape, Motion and Deformation Measurements: Basic Concepts, Theory and Applications. Springer, New York, 2009.

Taguchi, A., Murata, K., Nakamura, M., Nakano, T. (2011) Scale effect in the anisotropic deformation change of tracheid cells during water adsorption. Holzforschung 65:253–256.

Trtik, P., Dual, J., Keunecke, D., Mannes, D., Niemz, P., Stahli, P., Kaestner, A., Groso, A., Stampanoni, M. (2007) 3D imaging of microstructure of spruce wood. J. Struct. Biol. 159:46–55.

Valla, A., Konnerth, J., Keunecke, D., Niemz, P., Müller, U., Gindl, W. (2010) Comparison of two optical methods for contactless, full field and highly sensitive in plane deformation measurements using the example of plywood. Wood Sci. Technol. 45:755–765.

Wagenführ, R. Holzatlas. Fachbuchverlag Leipzig, 2000.